

# Revealing the $\text{EuCd}_2\text{As}_2$ Semiconducting Band Gap via n-Type La-Doping

Published as part of *Chemistry of Materials virtual special issue* "C. N. R. Rao at 90".

Ryan A. Nelson, Jesaiah King, Shuyu Cheng, Archibald J. Williams, Chris Jozwiak, Aaron Bostwick, Eli Rotenberg, Souvik Sasmal, I-Hsuan Kao, Aalok Tiwari, Natalie R. Jones, Chuting Cai, Emma Martin, Andrei Dolocan, Li Shi, Roland K. Kawakami, Joseph P. Heremans, Jyoti Katoch, and Joshua E. Goldberger\*



Cite This: *Chem. Mater.* 2024, 36, 7623–7632



Read Online

ACCESS |



Metrics & More

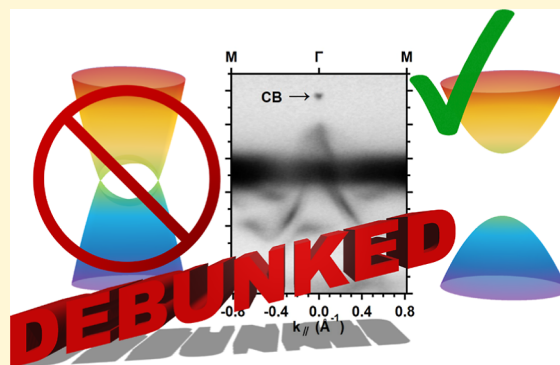


Article Recommendations



Supporting Information

**ABSTRACT:**  $\text{EuCd}_2\text{As}_2$  has attracted considerable interest as one of the few magnetic Weyl semimetal candidate materials, although recently, there have been emerging reports that claim it to have a semiconducting electronic structure. To resolve this debate, we established the growth of n-type  $\text{EuCd}_2\text{As}_2$  crystals to directly visualize the nature of the conduction band using angle-resolved photoemission spectroscopy (ARPES). We show that La-doping leads to n-type transport signatures in both thermopower and Hall effect measurements, in crystals with n-type doping levels of  $2\text{--}6 \times 10^{17} \text{ cm}^{-3}$ . Both p- and n-type-doped samples exhibit antiferromagnetic ordering at 9 K. ARPES experiments at 6 K clearly show the presence of the conduction band minimum at 0.8 eV above the valence band maximum, which is further corroborated by the observation of a 0.71–0.72 eV band gap in room temperature diffuse reflectance absorbance measurements. Together, these findings unambiguously show that  $\text{EuCd}_2\text{As}_2$  is indeed a semiconductor with a substantial band gap and not a topological semimetal.



$\text{EuCd}_2\text{As}_2$  is indeed a semiconductor with a substantial band gap and not a topological semimetal.

## INTRODUCTION

The realization of materials with topologically nontrivial electronic structures<sup>1–3</sup> has been a major thrust in solid-state research over the past decade. One such desired phase is the magnetic Weyl semimetal, wherein the band structure near the Fermi level is characterized by a pair of nodal band crossings with linear dispersions on top of the underlying magnetic order, enabling phenomena such as the chiral anomaly and its thermal analogue.<sup>4–7</sup> The chiral anomaly and thermal chiral anomaly feature large, nonsaturating negative electrical magnetoresistances and thermal magnetoresistances and thus hold great promise in electronic devices and thermal switching applications. However, efficient utilization of these transport phenomena requires materials in which the Fermi level is coincident with the nodal band crossings and that there are no other topologically trivial bands at this energy. Almost all magnetic Weyl semimetal candidates have either trivial or nontrivial bands near the topologically nontrivial nodal crossing, as is the case for materials such as  $\text{Co}_2\text{MnGa}$ ,  $\text{Mn}_3\text{Sn}$ , and  $\text{EuGa}_4$ .<sup>8–10</sup> Alternatively,  $\text{MnBi}_2\text{Te}_4$  is a well-known magnetic Weyl semimetal candidate that has the ideal electronic structure but is hindered by the challenge in growing single crystals with experimentally relevant thickness in the

cross-plane direction due to it being a peritectic phase with a  $<10^\circ\text{C}$  window of synthetic accessibility.<sup>11,12</sup> The identification and development of magnetic Weyl semimetals remain an important frontier in materials research.

Along these lines,  $\text{EuCd}_2\text{As}_2$  has been proposed as an attractive magnetic Weyl semimetal candidate due to its ideal band structure and robust synthetic accessibility.<sup>13</sup> From 2016 to 2023, most theoretical and experimental studies of  $\text{EuCd}_2\text{As}_2$  assumed that this material was semimetallic at room temperature and below, until forming a topological antiferromagnet below the Néel temperature ( $T_N$ ) of 9.5 K, with nodal crossings very close to the  $\Gamma$  point.<sup>13–22</sup> The Weyl semimetal state was thought to be accessible by forcing the structure to be ferromagnetic with polarization along the  $c$ -axis via a modest magnetic field ( $\sim 1.5 \text{ T}$ ).<sup>13,15</sup> The semimetallic nature was supported using a broad range of measurements.

Received: March 5, 2024

Revised: July 10, 2024

Accepted: July 11, 2024

Published: July 24, 2024



First, most in-plane resistivity measurements on single crystals remained below 100 m $\Omega$  cm (or <10<sup>-3</sup>  $\Omega$  m), often varying between about 5 and 50 m $\Omega$  cm and increasing slightly with temperature.<sup>13,17,21,23–26</sup> Both thermopower and Hall measurements indicated p-type doping,<sup>15,17,19,22,26–31</sup> with carrier concentrations that depended on the synthesis method, and ranged from about 10<sup>15</sup> to 10<sup>18</sup> cm<sup>-3</sup> in Sn flux to about 10<sup>20</sup> cm<sup>-3</sup> in salt (KCl/NaCl) flux.<sup>26,31–33</sup> The variation in hole concentrations is attributed to the differing levels of Eu vacancies.<sup>16,26</sup> Angle-resolved photoemission spectroscopy (ARPES) corroborated the inherent p-type doping as the Fermi level of all materials was within the valence band.<sup>15,16,21,22,26,32,34,35</sup> This hindered direct observation of the proposed semimetallic nature, namely, the presence of the conduction band minimum (CBM) that was expected to dip below the valence band maximum (VBM) at the  $\Gamma$  point by  $\sim$ 50 meV from calculations.<sup>15,21,22</sup> One previous ARPES study reported the presence of the CBM within 20 meV of the Fermi level, although the fact that this is close to the reported 5–30 meV energy resolution of the ARPES experiment introduces some ambiguity to this assignment.<sup>22</sup> The clear identification of the VBM and CBM by ARPES measurements of n-type samples would provide more compelling evidence of their semimetallic nature. Finally, optical reflectivity experiments show the presence of a low-energy plasma frequency below 350 cm<sup>-1</sup> and approach unity at the lowest energy, further supporting metallic behavior in these samples.<sup>23,36</sup> Low-temperature magneto-infrared spectroscopy measurements also showed an increase in reflectivity upon application of a magnetic field below  $T_N$ , along with the presence of field-dependent van Hove singularities, which together were attributed to the excitations between the overlapping CBM and VBM levels whose energies have a strong magnetic field dependence in a Weyl semimetal.<sup>37</sup>

Recently, Santos-Cottin et al. reported that EuCd<sub>2</sub>As<sub>2</sub> is actually a 0.77 eV semiconductor based on the growth of EuCd<sub>2</sub>As<sub>2</sub> using a higher-purity Eu metal source (4N) and a two-step seeded synthesis.<sup>35</sup> These higher-purity EuCd<sub>2</sub>As<sub>2</sub> crystals showed an insulating temperature dependence of resistivity with a 300 K value of around 3  $\times$  10<sup>3</sup> m $\Omega$  cm that rose over 6 orders of magnitude upon cooling to 10 K. Similarly, high-purity crystals have since been grown by other groups, and comparable insulating behavior has been observed.<sup>19,20,30,31</sup> It is important to point out that resistivity measurements alone are subject to possible error through the presence of nonohmic or insulating contact barriers. The insulating behavior was further indicated by optical reflectivity measurements, in which a low-energy reflectivity value of  $\sim$ 0.4 was observed in these lower doped samples, along with a strong absorption edge at 0.77 eV. Finally, pump–probe ARPES measurements that collected photoemission of the excited state from the 001 surface (using 37 eV probe excitation) indicated the presence of a long-lived state at 0.76 eV above the VBM, which was attributed to excitation to the CBM.<sup>35</sup> There was also a short-lived excitation at 0.13 eV above the Fermi level, which was attributed to excitation to the VBM and subsequent thermalization back to the Fermi level, implying appreciable p-type doping. It is important to point out that in density functional theory calculations that have predicted a Weyl semimetal electronic structure of EuCd<sub>2</sub>As<sub>2</sub>, the VBM and CBM cross within 0.1  $\text{\AA}^{-1}$  of  $\Gamma$  to give the Weyl nodes and the predicted  $\sim$ 50 meV overlap, whereas the difference in energy between the VBM and CBM at the  $A$

point (0 0  $\pi/c$ ) is  $\sim$ 0.7 eV (Figure S1).<sup>15,21,22</sup> Considering the large number of experiments that previously suggested EuCd<sub>2</sub>As<sub>2</sub> to be semimetallic, these results along with all previous studies require careful scrutiny of measurements and samples.

There is clearly extensive debate about the nature of the electronic structure of EuCd<sub>2</sub>As<sub>2</sub>. Accurate characterization of a narrow-band-gap semiconductor is often complicated by the presence of dopants or impurities. Consider the history of InN, for which early reports assigned the band gap as 1.9 eV.<sup>38</sup> This value was widely accepted until photoluminescence experiments revealed a true value of 0.7 eV.<sup>39,40</sup> Furthermore, the electronic structure of materials composed of unpaired d- or f-electrons have been notoriously difficult to model accurately using density functional theory due to the strong electron–electron correlations along with the high cost of using more accurate high-level functionals.<sup>41</sup> Because of the ambiguity inherent in all of the previously described measurements, the most definitive signature that would identify EuCd<sub>2</sub>As<sub>2</sub> as a semiconductor would be static ARPES measurements on an n-doped crystal at precisely the  $\Gamma$  point as this is where the CBM and VBM occur. This is what we report here.

Here, we establish that EuCd<sub>2</sub>As<sub>2</sub> is indeed a semiconductor with a 0.7–0.8 eV band gap, through the preparation and extensive characterization of n-type EuCd<sub>2</sub>As<sub>2</sub> crystals. We show that the incorporation of La into the Sn-flux synthesis leads to n-type thermopowers and Hall effect signatures. ARPES measurements at 6 K of potassium-dosed samples unambiguously show the CBM at 0.8 eV above the VBM, with no other states observed within the gap. Room-temperature diffuse reflectance absorbance measurements further confirm an optical band gap in both p-type and n-type samples around 0.71 eV. Overall, these experiments provide strong evidence that EuCd<sub>2</sub>As<sub>2</sub> is indeed a semiconductor.

## METHODS

Single crystals with lengths >3 mm and thicknesses >0.5 mm were synthesized using the previously reported Sn-flux synthesis procedure.<sup>16,42</sup> The elements Eu (4N, Glentham Life Sciences), Cd (5N, Thermo Scientific), As (5N, Thermo Scientific), and Sn (6N+, Thermo Scientific) were mixed in a Eu/Cd/As/Sn ratio of 1:2:2:10 inside Canfield crucibles. Sn was added to the crucible last to promote solubilization of all reagents. Care was taken to reduce the exposure of freshly cleaved Eu reagent to parts per million level oxidants. The reagent mixture was slowly heated to 900  $^{\circ}$ C over 24 h and then held at 900  $^{\circ}$ C for 20 h to allow full reagent diffusion before slowly cooling to 500  $^{\circ}$ C at 2  $^{\circ}$ C per hour to crystallize the EuCd<sub>2</sub>As<sub>2</sub> product. The molten flux was decanted via centrifugation at 500  $^{\circ}$ C to collect the product crystals.<sup>43</sup> Sn flux was further removed by fine sanding of the surfaces. To grow n-type crystals, 1–10 mol % of the Eu was replaced by La (Strem, 3N). It is important to note that the actual concentration of La that incorporates into the single crystals is much less than 1%, as will be described in the Results and Discussion section.

Thermoelectric transport measurements of EuCd<sub>2</sub>As<sub>2</sub> single crystals were conducted along the in-plane direction. Measurements from 80 to 400 K were conducted using a Janis SuperTran cryostat system (Lakeshore) with liquid nitrogen as the cryogen. The maximum field used with this instrument was  $\pm$ 1.4 T. Single crystals were mounted in cryostat measurement devices constructed according to the described device schematic using conductive silver-based epoxy (EPO-TEK H20E). Brass sheets were used as current spreaders, providing a uniform electrical and thermal current flow. An insulating alumina baseplate acted as the mounting plate and heat sink. Conductive epoxy was also used to secure measurement leads directly to the crystals. The measurement leads were 20  $\mu$ m copper wires. The

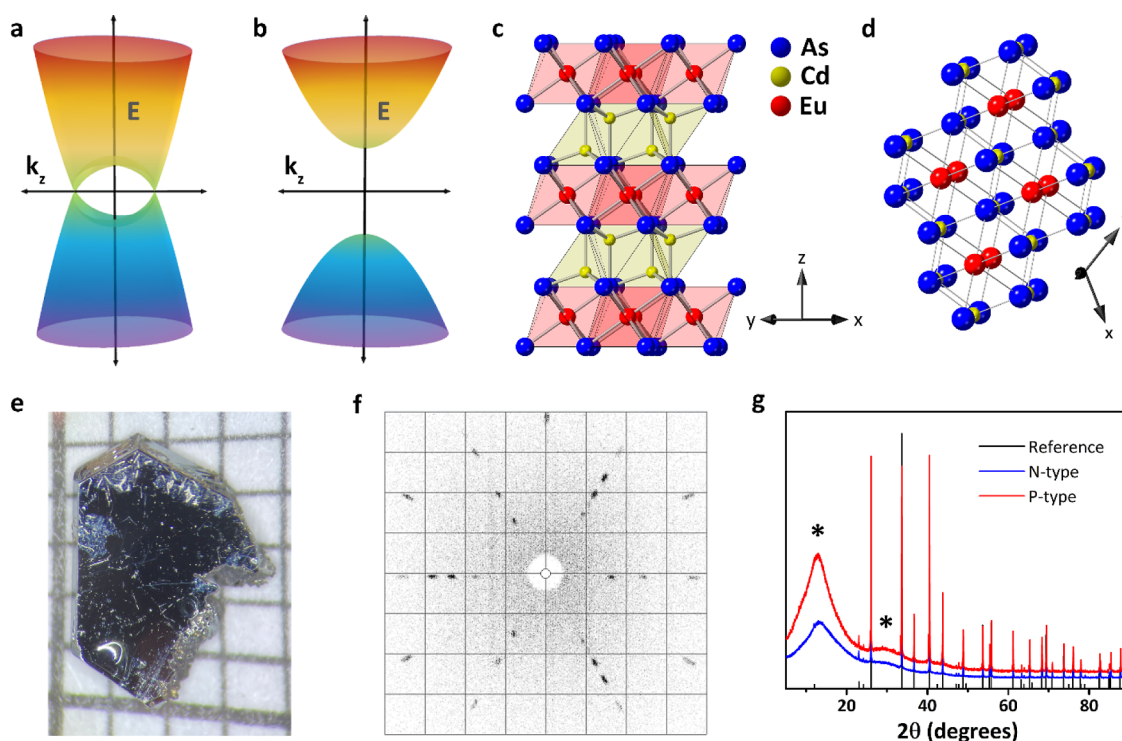


**Figure 1.** (a) Qualitative three-dimensional band structure of an ideal Weyl semimetal with linear dispersion near the Weyl nodes lying along the  $k_z$  axis. (b) Qualitative three-dimensional band structure of a trivial direct-gap semiconductor. In schematics (a) and (b), the  $k_z$  directions lie horizontally. In (a), the energy gap in the zone center has been reported to be  $\sim 50$  meV, whereas in (b), the energy gap in the zone center is reported to be 0.8 eV. (c) Crystal structure of  $\text{EuCd}_2\text{As}_2$ , as viewed along the 110-axis with the 001-axis aligned vertically. The yellow highlighted layers represent the edge-sharing  $\text{CdAs}_4$  tetrahedra sandwiched between the layers of edge-sharing  $\text{EuAs}_6$  octahedra in red. (d) Crystal structure of  $\text{EuCd}_2\text{As}_2$ , as viewed along the 001-axis to emphasize the trigonal symmetry. (e) Image of a  $\sim 4 \times 3$  mm<sup>2</sup> p-type  $\text{EuCd}_2\text{As}_2$  crystal with the 001-axis perpendicular to the plane of the page. (f) Laue backscattered diffraction pattern measured along the 001-axis of a p-type  $\text{EuCd}_2\text{As}_2$  sample showing the trigonal symmetry. (g) Powder X-ray diffraction of ground up crystals of p-type and n-type  $\text{EuCd}_2\text{As}_2$ . (\*) The large hump at low angles is a background feature caused by reflection from the low-volume acrylic sample holder.

type-T thermocouples were made using the same 20  $\mu\text{m}$  copper wire as well as Constantan wire. For electrical transport measurements below 80 K, a cryogen-free Quantum Design Physical Properties Measurement System (PPMS) was employed. The maximum field for this instrument was  $\pm 14$  T. PPMS measurement devices were constructed in much the same way as the cryostat devices but did not include a resistive heater or thermocouples. These devices were then mounted and wired to a resistivity puck (LakeShore). No thermal measurements were performed on the QD PPMS instrument given the absence of a thermal transport accessory.

The synchrotron-based ARPES measurements were performed at beamline 7.0.2 “MAESTRO” of the Advanced Light Source at Berkeley National Lab. The photoelectrons were collected using a Scienta Omicron R4000 hemispherical electron analyzer, which provided energy and momentum resolution better than 30 meV and 0.01  $\text{\AA}^{-1}$ , respectively. The  $\text{EuCd}_2\text{As}_2$  bulk crystal samples were cleaved in situ and measured at a base temperature of 6 K. A full reciprocal space map using a photon energy scan was performed before potassium dosing to determine the high-symmetry planes in the momentum space, and 130 eV photon energy was selected to access the plane. The effective electron concentration induced by potassium dosing is estimated following the methods described by Katoch et al., and the details are presented in the [Supporting Information](#).<sup>44</sup>

Magnetic susceptibility and magnetization data were collected via an MPMS3 superconducting quantum interference device (SQUID) magnetometer by Quantum Design. Magnetic susceptibility data acquisition occurred over a temperature range from 2 to 300 K. Small crystals ( $< 5$  mg) of  $\text{EuCd}_2\text{As}_2$  were encapsulated by Kapton tape and affixed to the desired field orientation of measurement in a plastic straw by another piece of Kapton tape. After cooling to 2 K with no

applied field, zero-field cooled magnetic susceptibility measurements were conducted under an applied field of 500 Oe all the way to 300 K. Then, the sample was returned to 2 K under the same 500 Oe measurement field, and magnetic susceptibility measurements were again conducted under a 500 Oe field up to 300 K. The magnetization vs field data were collected at 2 K by cycling the applied field in 1000 Oe increments, starting from 0 T, between +4 T and  $-4$  T two times. The crystals used for magnetic characterization were cleaved as small fragments of larger single crystals so as not to overrange the SQUID magnetometer. Thus, the in-plane and cross-plane crystal dimensions were comparable, and no self-demagnetization correction factor was applied to the data.

Infrared spectroscopy was performed by using a PerkinElmer Frontier dual-range IR spectrometer under a nitrogen atmosphere. The infrared reflectance spectra were acquired in diffuse reflectance infrared Fourier transform spectroscopy (DRIFTS) mode. All material was diluted in KBr that was flame-dried in a quartz ampule, and the same salt was used as the background. Tauc/Davis–Mott relations were applied to the reflectance data assuming an allowed direct transition and a three-dimensional density of states.

Time-of-flight secondary ion mass spectrometry (ToF-SIMS) was performed at the Texas Materials Institute at the University of Texas in Austin. The data collected under negative polarity used a 1 kV  $\text{O}_2^+$  ion beam with a beam current of about 41 nA. The raster scanned areas were 300  $\mu\text{m} \times 300 \mu\text{m}$ . The depth profile data were collected sequentially using a 30 keV  $\text{Bi}^+$  analysis beam with a raster scanned area equal to 100  $\mu\text{m} \times 100 \mu\text{m}$  centered within the sputtered area. The analysis beam current was 0.3 pA. Positive polarity data were collected in the same way, except that the sputtering beam was a 0.5 kV  $\text{Cs}^+$  ion beam with a similar 40 nA beam current. The p-type and n-type  $\text{EuCd}_2\text{As}_2$  samples, including n-type samples grown with initial

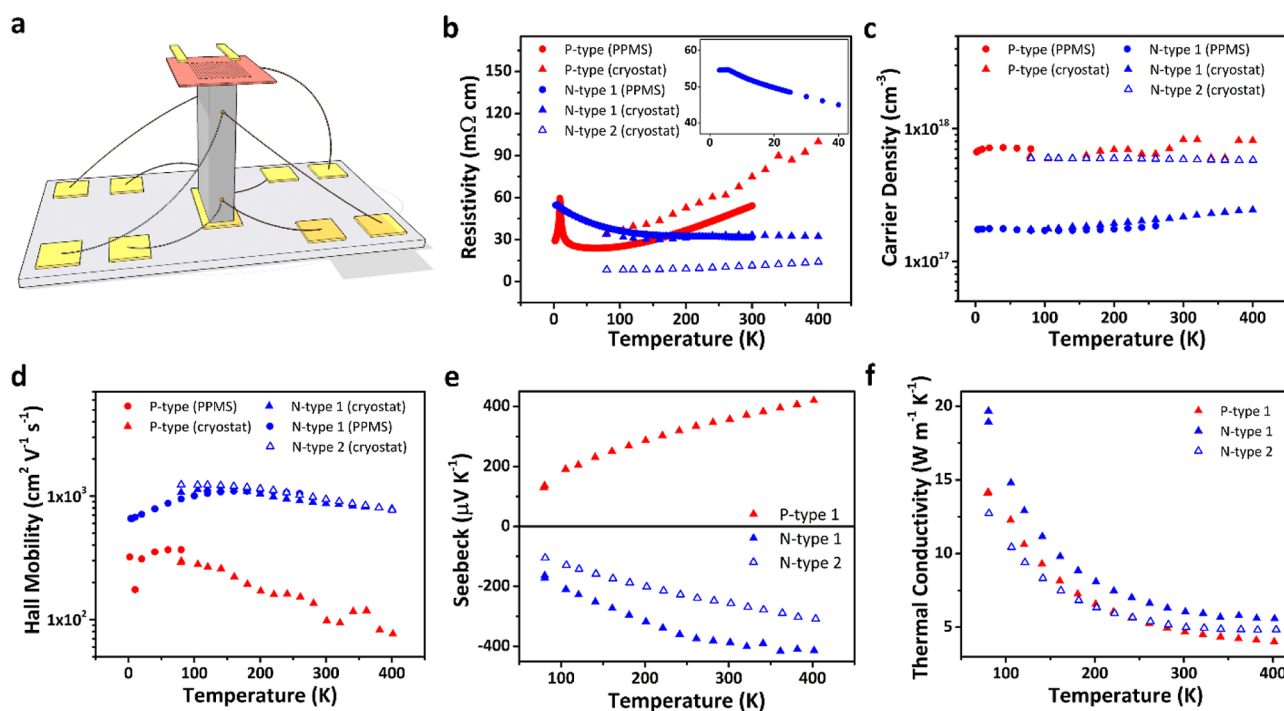


**Figure 2.** (a) Schematic diagram of a typical cryostat device used to measure the thermal and electrical transport properties of EuCd<sub>2</sub>As<sub>2</sub> single crystals. The yellow slabs represent brass contacts and current spreaders. The red colored slab at the top represents the resistive heater used for establishing a thermal gradient. The gray vertical block in the middle represents the single crystal of EuCd<sub>2</sub>As<sub>2</sub>, and the light-gray slab (bottom) represents the alumina baseplate. (b–f) Transport data measured on both p- and n-type EuCd<sub>2</sub>As<sub>2</sub> single crystals. Hall data are extracted assuming single carrier transport. Circles represent PPMS data, while triangles correspond to cryostat data. (b) Temperature-dependent resistivity measured from <10 to 400 K. (c) Temperature-dependent carrier density measured from <10 to 400 K. (d) Temperature-dependent Hall mobility measured from <10 to 400 K. (e) Temperature-dependent thermopower measured from about 80 to 400 K. (f) Temperature-dependent thermal conductivity measured from about 80 to 400 K.

La/Eu molar ratios of 1:99 and 10:90, were sputtered and measured using ToF-SIMS. The sputtering depth varied from 0.3 to 5.6 μm.

## RESULTS AND DISCUSSION

The debate about the nature of EuCd<sub>2</sub>As<sub>2</sub> is centered on whether there is band overlap between the CBM and VBM allowing for a Weyl semimetal state with ferromagnetic alignment of the spins (Figure 1a), or if it is indeed a trivial semiconductor (Figure 1b). Herein, we seek to answer that question conclusively by the growth and ARPES characterization of EuCd<sub>2</sub>As<sub>2</sub> single crystals. Specifically, ARPES measurements on samples in which the conduction band is clearly visible (i.e., n-doped) without the ambiguity inherent in a pump–probe experiment offer the most compelling answer to this question. Photo-ARPES requires photoexcitation to populate and visualize the states in the conduction band, whereas visualizing the conduction band in a ground state via n-type doping after confirming the location along *k<sub>z</sub>* is a more precise observation. To accomplish this, EuCd<sub>2</sub>As<sub>2</sub> crystals were synthesized in Sn flux using high-purity reagents (4N or greater, except 3N for La), which resulted in the growth of batches of crystals that were either p-type or n-type with carrier densities on the order of 10<sup>17</sup>–10<sup>18</sup> cm<sup>-3</sup> at room temperature based on Hall measurements. ToF-SIMS was able to detect the incorporation of La in more highly doped n-type crystals with carrier densities around 6 × 10<sup>17</sup> cm<sup>-3</sup> (Figure S2). ToF-SIMS revealed no significant compositional differences between the p-type and the more lightly doped n-type samples with carrier densities of 2 × 10<sup>17</sup> cm<sup>-3</sup> (Figures S3 and S4), indicating that the dopant concentration was likely

below the ToF-SIMS detection limit. n-Type doping behavior was reproduced across multiple batches of crystals when La was intentionally incorporated into the reaction mixture. In contrast, crystals grown with >1% Li, Na, Se, Gd, Dy, Sm, or Yb added to the reaction mixture resulted in p-type transport signatures. A simple electron counting approach would suggest that any trivalent lanthanide substituted onto a metal site would donate one more electron than the divalent Eu or Cd. However, the observation that the other trivalent lanthanides mentioned do not lead to n-type doping behavior implies either a lack of incorporation into EuCd<sub>2</sub>As<sub>2</sub> or a more complex doping mechanism that does not lead to n-type behavior. A detailed understanding of rare earth doping behavior merits future study.

EuCd<sub>2</sub>As<sub>2</sub> has a crystal structure (*P* $\bar{3}m1$ ) composed of layers of edge-sharing CdAs<sub>4</sub> tetrahedra, sandwiched between single-octahedron-thick layers of edge-sharing EuAs<sub>6</sub> octahedra (Figure 1c). Using an ionic bonding formality, the Eu and Cd-oxidation states are both 2+, while that of As is 3-. The trigonal symmetry becomes clear by viewing the structure along the 001-axis (Figure 1d) and is manifested in the crystal growth shape (Figure 1e) and Laue backscattered diffraction pattern (Figure 1f). Phase confirmation by powder X-ray diffraction shows that both p-type and n-type EuCd<sub>2</sub>As<sub>2</sub> retain the expected crystal structure (Figure 1g). The lattice parameters were refined to values of *a* = 4.43979(5) Å and *c* = 7.32690(6) Å for p-type EuCd<sub>2</sub>As<sub>2</sub> and refined to *a* = 4.44012(9) Å and *c* = 7.32664(10) Å for n-type EuCd<sub>2</sub>As<sub>2</sub> (Figure S4). These values are in excellent agreement with previously reported values and show no significant structural

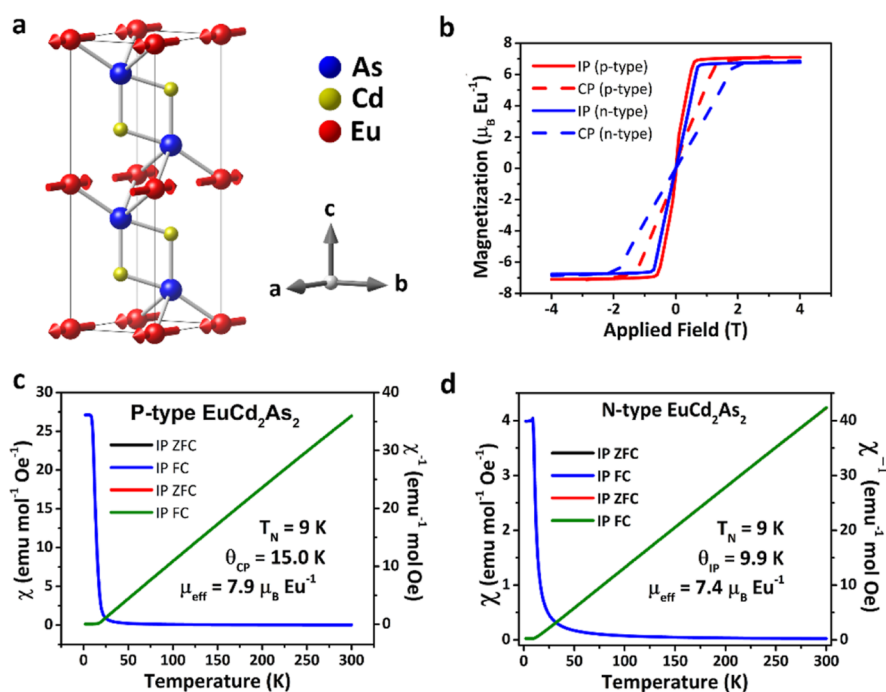


**Figure 3.** (a) Magnetic structure of AFM EuCd<sub>2</sub>As<sub>2</sub> showing in-plane ferromagnetic exchange and cross-plane AFM exchange. (b) Field-dependent magnetization of both p- and n-type EuCd<sub>2</sub>As<sub>2</sub>. (c) Temperature-dependent magnetic susceptibility and inverse magnetic susceptibility of p-type EuCd<sub>2</sub>As<sub>2</sub> measured from 2 to 300 K. (d) Temperature-dependent magnetic susceptibility and inverse magnetic susceptibility of n-type EuCd<sub>2</sub>As<sub>2</sub> measured from 2 to 300 K. The Curie–Weiss fitting was taken over the range from 11 to 300 K for both p-type and n-type samples. In (c) and (d), the FC and ZFC curves are superimposable.

difference between the p- and n-type samples.<sup>13,14,17,19,20,23,30,35,45–49</sup>

Thermoelectric transport properties were measured using both a Janis SuperTran cryostat system (Figure 2a) and a Quantum Design PPMS. The temperature-dependent resistivities obtained for all samples of EuCd<sub>2</sub>As<sub>2</sub> are similar in magnitude to previous reports on the metallic samples (Figure 2b). The p-type resistivity shows a sharp cusp at the magnetic transition temperature ( $T_N \cong 9.2$  K), peaking just under 60 mΩ cm and ranging from about 29 mΩ cm at 2 K to nearly 100 mΩ cm at 400 K. The cusp at the magnetic transition has been observed in nearly all previous p-type transitions and arises due to carrier scattering with the spinwaves that emerge below this temperature. The n-type resistivities show a much smaller cusp near the magnetic transition (Figure 2b inset). Also, the n-type samples, although close in magnitude, have varying temperature coefficients of resistivities. One crystal (crystal 1) had a modest decrease in resistivity from just over 55 mΩ cm at 3 K to about 32 mΩ cm at 400 K, while a second crystal (crystal 2) showed a small increase in resistivity from about 8 mΩ cm at 80 K to just over 12 mΩ cm. The cryostat data and PPMS data show good overlap and appear consistent over the measured temperature range. Overall, this resistivity range is in good agreement with previous reports and fits a degenerately doped-semiconductor picture for EuCd<sub>2</sub>As<sub>2</sub>.<sup>13,17,21,23–26</sup>

The carrier concentrations were extracted from the Hall resistivity curves (Figure S5) using a single carrier model. The temperature-dependent carrier densities observed for all samples of EuCd<sub>2</sub>As<sub>2</sub> are plotted in Figure 2c. The p-type carrier densities fall in a narrow range from  $6.0 \times 10^{17}$  cm<sup>-3</sup> at low temperature to  $8.3 \times 10^{17}$  cm<sup>-3</sup> at high temperature. The n-type carrier densities fall into similarly narrow ranges. Crystal

1 has a doping level of  $1.7 \times 10^{17}$  cm<sup>-3</sup> at low temperatures that rises to  $2.4 \times 10^{17}$  cm<sup>-3</sup> at high temperatures. Crystal 2 stays nearly constant across the measured temperature range of  $6 \times 10^{17}$  cm<sup>-3</sup>. These carrier densities are 1–3 orders of magnitude lower than the previous reports claiming semimetallic behavior.<sup>26,32</sup> The nearly temperature-independent carrier densities and resistivities in both the p-type and n-type samples suggest that these EuCd<sub>2</sub>As<sub>2</sub> crystals are degenerately doped. For comparison, Ge, a semiconductor with a similar band gap, also becomes degenerately doped at  $10^{17}$  cm<sup>-3</sup>.<sup>50</sup>

Hall mobility was derived from the Hall coefficient and electrical resistivity. The temperature-dependent Hall mobilities are plotted in Figure 2d. The p-type mobility is 322 cm<sup>2</sup> V<sup>-1</sup> s<sup>-1</sup> at 2 K and rises to 368 cm<sup>2</sup> V<sup>-1</sup> s<sup>-1</sup> at 80 K before finally falling to 76.5 cm<sup>2</sup> V<sup>-1</sup> s<sup>-1</sup> at about 400 K. The n-type mobility for crystal 1 is higher, beginning at 658 cm<sup>2</sup> V<sup>-1</sup> s<sup>-1</sup> at 3.5 K before reaching a maximum value of 1144 cm<sup>2</sup> V<sup>-1</sup> s<sup>-1</sup> at 120 K. Finally, the n-type mobility drops to 796 cm<sup>2</sup> V<sup>-1</sup> s<sup>-1</sup> at 400 K. n-Type crystal 2 has comparable mobilities. The fact that the n-type crystals have similar doping levels but higher mobilities than the p-type crystals is consistent with the behavior of virtually all known semiconductors as conduction electrons originate in bands with more antibonding character that tend to be more disperse resulting in higher mobility.<sup>51</sup> Additionally, the magnitudes of the observed mobilities are more consistent with a semiconductor than a topologically trivial metal. The electron effective mass determined by the method of the four coefficients<sup>52</sup> was found to be 0.07 m<sub>e</sub> at low temperature.

The temperature-dependent thermopowers shown in Figure 2e were measured down to 80 K. The signs of the thermopower, along with the slopes of the Hall resistivity curves, allow unambiguous assignment of p- and n-type doping

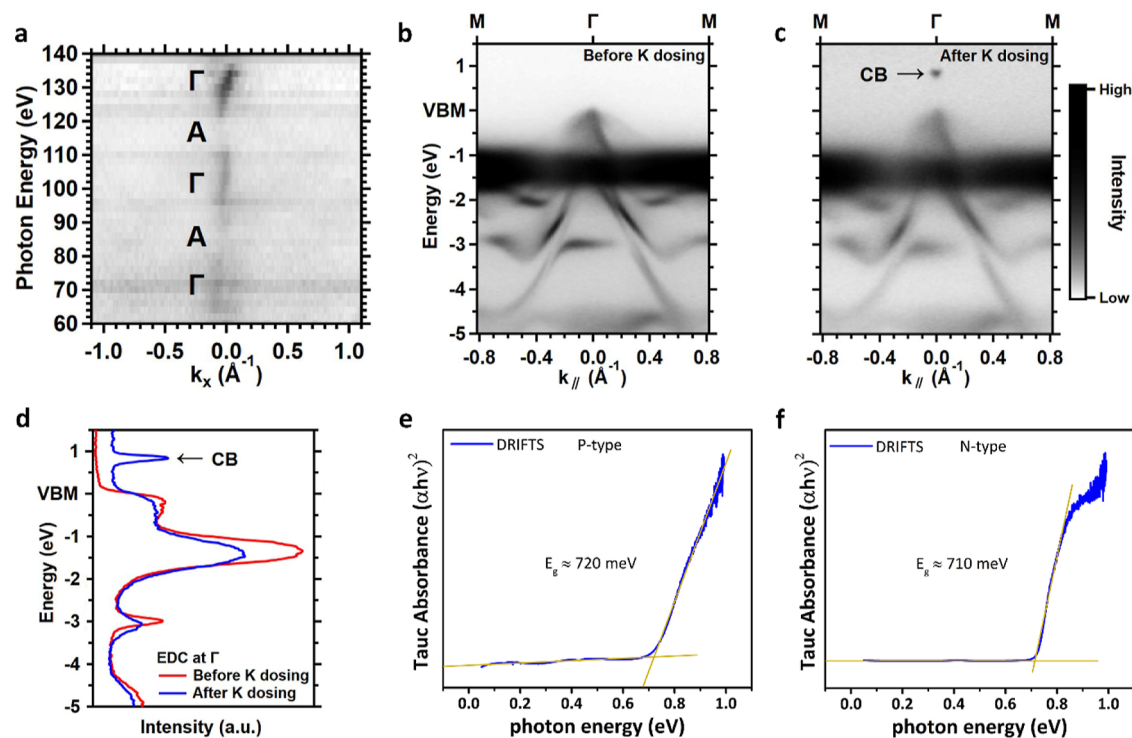


**Figure 4.** (a) Energy-dependent Fermi surface mapping along the cross-plane A- $\Gamma$ -A direction ( $k_x$ -axis) from 60 to 140 eV. The  $k_x$ -axis lies in the M- $\Gamma$ -M in-plane direction. 130 eV was selected to access the  $k_z = 0$  plane. (b) Intensity plot for ARPES measured at 6 K on an n-type sample of  $\text{EuCd}_2\text{As}_2$  showing the dispersion over the M- $\Gamma$ -M direction on a cleaved 001-facet. (c) ARPES intensity plot measured on the same n-type sample at 6 K after dosing the surface with evaporated potassium metal (K-dosing). Note that the bottom of the conduction band is clearly visible at  $\sim 800$  meV above the top of the valence band. (d) Energy distribution curves showing the energy-dependent density of states at  $\Gamma$ . Note the clear emergence of conduction band states at about 800 meV after K-dosing. (e) DRIFTS Tauc plot measured on p-type  $\text{EuCd}_2\text{As}_2$  assuming an allowed 3D direct transition. (f) DRIFTS Tauc plot measured on n-type  $\text{EuCd}_2\text{As}_2$  assuming an allowed 3D direct transition.

for the  $\text{EuCd}_2\text{As}_2$  samples. The data are nearly symmetric about the zero line in the temperature-dependent thermopower, with p-type thermopowers rising from  $130 \mu\text{V K}^{-1}$  at about 80 K to  $420 \mu\text{V K}^{-1}$  at about 400 K. The p-type thermopowers compare well with previous reports.<sup>17</sup> The n-type thermopower for crystal 1 on the other hand drops from  $-164 \mu\text{V K}^{-1}$  at around 80 K to about  $-415 \mu\text{V K}^{-1}$  near 400 K. The thermopower values in the more highly doped crystal 2 have lower magnitudes, ranging from  $-105$  to  $-308 \mu\text{V K}^{-1}$  from 80 to 400 K, respectively.

Temperature-dependent thermal conductivity was measured from 80 to 400 K. The temperature-dependent thermal conductivities of p-type and n-type  $\text{EuCd}_2\text{As}_2$  have no significant differences. Both samples clearly show the expected features for a lattice-dominated thermal conductivity, namely, the  $1/T$  Umklapp phonon-phonon scattering trend with temperature. The p-type thermal conductivity at 80 K is about  $14 \text{ W m}^{-1} \text{ K}^{-1}$  and drops off to about  $4 \text{ W m}^{-1} \text{ K}^{-1}$  at 400 K. The n-type 80 K values are about  $20 \text{ W m}^{-1} \text{ K}^{-1}$ , falling to about  $5.5 \text{ W m}^{-1} \text{ K}^{-1}$  at 400 K. These values are all within the errors in the measurements and agree well with previously reported thermal conductivities.<sup>17</sup> An initial estimation of the 400 K thermoelectric figure of merit ( $zT$ ) from the Seebeck coefficients, electrical resistivities, and thermal conductivities was 0.018–0.056 across all samples (Table S1). Improved thermoelectric performance is possible with further optimization and derivatization. However, because  $\text{EuCd}_2\text{As}_2$  is composed of the toxic elements of cadmium and arsenic,

terrestrial thermoelectric applications of this material would be niche at best.

The magnetic behavior of both p- and n-type crystals was investigated by SQUID magnetometry to reveal any doping-dependent differences in magnetism. Previous reports have demonstrated that the magnetic ground state of p-type  $\text{EuCd}_2\text{As}_2$  is antiferromagnetic (AFM) with an in-plane A-type ordering (Figure 3a), and that  $\text{EuCd}_2\text{As}_2$  can be fully ferromagnetically polarized in modest fields of  $< 2$  T.<sup>13,14,23</sup> Magnetization vs applied field measurements at 2 K on both p-type and n-type crystals corroborate the AFM ground state, showing an absence of hysteresis, and both give polarization to the ferromagnetic state at a field of about 0.6–0.8 T for in-plane and about 1.3–2.0 T for cross-plane. The saturation moments from the magnetization data on p-type and n-type samples are  $7.1 \mu_B \text{ Eu}^{-1}$  and  $6.8 \mu_B \text{ Eu}^{-1}$ , respectively. A previous study evaluating  $\text{EuCd}_2\text{As}_2$  crystals with different p-doping levels found that the saturation moment is suppressed with increased p-doping.<sup>16</sup> The decreased saturation moment in our n-doped sample corroborates the observation that the saturation moment is quite sensitive to the doping level. Magnetic susceptibility measurements from 2 to 300 K further confirmed the AFM ground state of both p-type and n-type samples, both of which have a  $T_N$  of 9 K (Figure 3c and d). The p-type ZFC and FC susceptibility peaks are at  $26.8 \text{ emu mol}^{-1} \text{ Oe}^{-1}$ . The n-type magnetic susceptibility also remains practically identical from ZFC to FC, with both peaking above 4  $\text{emu mol}^{-1}$  of  $\text{Oe}^{-1}$ . A Curie-Weiss fit was applied to the temperature range from 11 K – 300 K for the inverse magnetic

susceptibility yielding positive Curie–Weiss temperatures of 15.0 and 9.9 K for p-type and n-type, respectively. The positive Curie–Weiss temperature is likely due to the strength of the ferromagnetic short-range interactions and has been seen previously in p-type  $\text{EuCd}_2\text{As}_2$  as well as other materials containing  $\text{Eu}^{2+}$ .<sup>13,14,23,53–55</sup> The high-temperature local saturation moment is also evident in the magnetic susceptibility, giving values of  $7.9 \mu_{\text{B}} \text{Eu}^{-1}$  for p-type  $\text{EuCd}_2\text{As}_2$  and  $7.4 \mu_{\text{B}} \text{Eu}^{-1}$  for the n-type. Further magnetic studies are required to fully understand the effect of La n-type doping on the magnetic properties of  $\text{EuCd}_2\text{As}_2$ .

To answer the question of whether  $\text{EuCd}_2\text{As}_2$  is a topological semimetal or a trivial insulator, we performed ARPES measurements on n-type  $\text{EuCd}_2\text{As}_2$  crystals. The  $\text{EuCd}_2\text{As}_2$  bulk crystals are cleaved in situ and measured at  $T = 6$  K. This temperature was chosen because it corresponds to the minimum temperature of the instrumentation and is below the  $T_{\text{N}}$  of 9.5 K, and previous ARPES studies show that changes in the valence band structure due to the AFM order emerge between 5 and 8 K.<sup>21</sup> Figure 4a shows the photon energy-dependent Fermi surface mapping along the A- $\Gamma$ -A direction from 60 to 140 eV before potassium dosing. This allows for determining the photon energies that corresponded to  $k_z = 0$  and  $k_z = \pi/c$ . Subsequently, 130 eV was selected when collecting further ARPES spectra as this approximately corresponds to  $k_z = 0$ . Figure 4b shows the ARPES spectrum measured along the M- $\Gamma$ -M direction on the 001-facet, while the K- $\Gamma$ -K ARPES spectrum is shown in Figure S7 for comparison.

The VBM is located at the  $\Gamma$  point, with a cone-like E vs k dispersion extending to about  $-0.8$  eV, below the VBM. Between  $-0.8$  and  $-2.0$  eV, the photoemission spectrum is dominated by flat bands spreading across the entire Brillouin zone. These bands originate from Eu 4f electrons. All these features are consistent with previous ARPES studies on  $\text{EuCd}_2\text{As}_2$  single crystals.<sup>15,16,21</sup> To directly visualize the conduction band, in situ potassium dosing was performed as it has been shown in other semiconductors that the CBM cannot be detected via ARPES at such a low n-doping level.<sup>56</sup> The ARPES spectrum after in situ potassium dosing is shown in Figure 4c. It is clear that an additional photoemission signal appears at the  $\Gamma$  point, with the maximum intensity located at about  $+0.8$  eV above the VBM. The photon energy-dependent Fermi surface mapping was not repeated after potassium dosing; however, all bands below 0 eV, as shown in Figure 4b and c, are essentially superimposable to one another, which implies negligible shifts in  $k_x$ ,  $k_y$ , or  $k_z$  following dosing. Given that there are no other bands observed between the VBM and this new signal at  $+0.8$  eV, the new band must be the CBM, which is only visible when there is sufficient population of electrons in the conduction band. While a topological semimetallic electronic structure would also result in the appearance of a gap between a lower-energy CBM and a higher-energy VBM (Figure 1a), an 800 meV semimetallic band overlap is over an order of magnitude larger than the overlap predicted for  $\text{EuCd}_2\text{As}_2$  ( $\sim 50$  meV).<sup>15,21,22</sup> Furthermore, calculations predicted the nodal crossings to occur at a  $k_z$  with  $0.1 \text{ \AA}^{-1}$  of the  $\Gamma$  point.<sup>22</sup> Together, this indicates that n-type  $\text{EuCd}_2\text{As}_2$  is a magnetic insulator instead of a topological semimetal. Figure 4d plots the energy distribution curves before (red) and after (blue) potassium dosing, giving the density of states as a function of energy. Fitting these curves at the  $\Gamma$  point using Lorentzian line shapes yields a band gap of

$\sim 0.8$  eV for our  $\text{EuCd}_2\text{As}_2$  samples with an effective electron concentration  $n_e = 6 \times 10^{18} \text{ cm}^{-3}$  after potassium dosing (Figure S8). To corroborate the band gap, DRIFTS measurements were collected on powders of both p-type and n-type  $\text{EuCd}_2\text{As}_2$ , and the Tauc/Davis–Mott relations were applied by assuming a three-dimensional density of states. Figure 4e and f shows the Tauc plots for p-type and n-type  $\text{EuCd}_2\text{As}_2$ , respectively. The band edges are clearly visible and extrapolated to 0.72 eV for p-type and 0.71 eV for n-type, in good agreement with the ARPES gap considering the DRIFTS data were collected at room temperature while the ARPES spectrum was collected at 6 K. The reflectance data are also in excellent agreement with previous reports showing an absorbance edge at  $\sim 0.75$  eV.<sup>31,35</sup>

## CONCLUSIONS

These results directly establish the semiconducting nature of  $\text{EuCd}_2\text{As}_2$  with a 0.7–0.8 eV band gap, through the growth and characterization of n-type  $\text{EuCd}_2\text{As}_2$  crystals. Incorporation of La into the Sn-flux synthesis as a dopant led to n-type thermopower and Hall effect signatures. The CBM was observed 0.8 eV above the VBM at 6 K through ARPES measurements, with no other states observed within the gap. Room-temperature diffuse reflectance absorbance measurements further confirmed a 0.71–0.72 eV optical band gap. Together, this corroborates the recent reports of semiconducting behavior and, with such a large band gap, precludes the possibility of realizing Weyl semimetallic behavior in  $\text{EuCd}_2\text{As}_2$  under most accessible experimental conditions. These results indicate that the realization of magnetic Weyl semimetals, and the scientifically and technologically intriguing phenomena that they may exhibit, will require further materials exploration and much more grounded expectations.

## ASSOCIATED CONTENT

### Supporting Information

The Supporting Information is available free of charge at <https://pubs.acs.org/doi/10.1021/acs.chemmater.4c00656>.

The predicted Weyl semimetal  $\text{EuCd}_2\text{As}_2$  band structure, ToF-SIMS data, Rietveld refinements of both p- and n-type  $\text{EuCd}_2\text{As}_2$ , Hall resistivity curves, and additional ARPES data (PDF)

## AUTHOR INFORMATION

### Corresponding Author

Joshua E. Goldberger – Department of Chemistry and Biochemistry, the Ohio State University, Columbus, Ohio 43210, United States; Department of Materials Science and Engineering, the Ohio State University, Columbus, Ohio 43210, United States; [orcid.org/0000-0003-4284-604X](https://orcid.org/0000-0003-4284-604X); Email: [goldberger@chemistry.ohio-state.edu](mailto:goldberger@chemistry.ohio-state.edu)

### Authors

Ryan A. Nelson – Department of Chemistry and Biochemistry, the Ohio State University, Columbus, Ohio 43210, United States; [orcid.org/0000-0003-0763-1094](https://orcid.org/0000-0003-0763-1094)

Jesaiah King – Department of Chemistry and Biochemistry, the Ohio State University, Columbus, Ohio 43210, United States

Shuyu Cheng – Department of Physics, the Ohio State University, Columbus, Ohio 43210, United States

**Archibald J. Williams** – Department of Chemistry and Biochemistry, the Ohio State University, Columbus, Ohio 43210, United States

**Chris Jozwiak** – Advanced Light Source, E.O. Lawrence Berkeley National Laboratory, Berkeley, California 94720, United States; [orcid.org/0000-0002-0980-3753](https://orcid.org/0000-0002-0980-3753)

**Aaron Bostwick** – Advanced Light Source, E.O. Lawrence Berkeley National Laboratory, Berkeley, California 94720, United States

**Eli Rotenberg** – Advanced Light Source, E.O. Lawrence Berkeley National Laboratory, Berkeley, California 94720, United States; [orcid.org/0000-0002-3979-8844](https://orcid.org/0000-0002-3979-8844)

**Souvik Sasmal** – Department of Physics, Carnegie Mellon University, Pittsburgh, Pennsylvania 15213, United States

**I-Hsuan Kao** – Department of Physics, Carnegie Mellon University, Pittsburgh, Pennsylvania 15213, United States; [orcid.org/0000-0003-1790-1254](https://orcid.org/0000-0003-1790-1254)

**Aalok Tiwari** – Department of Physics, Carnegie Mellon University, Pittsburgh, Pennsylvania 15213, United States

**Natalie R. Jones** – Department of Chemistry and Biochemistry, the Ohio State University, Columbus, Ohio 43210, United States

**Chuting Cai** – Materials Science and Engineering Program, The University of Texas at Austin, Austin, Texas 78712, United States

**Emma Martin** – Department of Mechanical Engineering, The University of Texas at Austin, Austin, Texas 78712, United States

**Andrei Dolocan** – Texas Materials Institute, The University of Texas at Austin, Austin, Texas 78712, United States; [orcid.org/0000-0001-5653-0439](https://orcid.org/0000-0001-5653-0439)

**Li Shi** – Materials Science and Engineering Program, The University of Texas at Austin, Austin, Texas 78712, United States; Department of Mechanical Engineering, The University of Texas at Austin, Austin, Texas 78712, United States; [orcid.org/0000-0002-5401-6839](https://orcid.org/0000-0002-5401-6839)

**Roland K. Kawakami** – Department of Physics, the Ohio State University, Columbus, Ohio 43210, United States; [orcid.org/0000-0003-0245-9192](https://orcid.org/0000-0003-0245-9192)

**Joseph P. Heremans** – Department of Physics, Department of Mechanical and Aerospace Engineering, and Department of Materials Science and Engineering, the Ohio State University, Columbus, Ohio 43210, United States; [orcid.org/0000-0003-3996-2744](https://orcid.org/0000-0003-3996-2744)

**Jyoti Katoch** – Department of Physics, Carnegie Mellon University, Pittsburgh, Pennsylvania 15213, United States

Complete contact information is available at:  
<https://pubs.acs.org/10.1021/acs.chemmater.4c00656>

### Author Contributions

The manuscript was written through contributions of all authors. All authors have given approval to the final version of the manuscript.

### Notes

The authors declare no competing financial interest.

### ACKNOWLEDGMENTS

This work was primarily supported by the ONR MURI “Extraordinary electronic switching of thermal transport” (grant no. N00014-21-1-2377) for J.E.G., R.A.N., N.R.J., J.C.K., L.S., J.P.H., E.M., and C.C. This research was partially supported by the Center for Emergent Materials, an NSF

MRSEC, under award no.DMR-2011876, for A.J.W., J.K., R.K.K., and S.C. J.K. also acknowledges funding from the U.S. Department Office of Science, Office of Basic Sciences, of the U.S. Department of Energy under award no. DE-SC0020323. This research used resources of the Advanced Light Source, which is a DOE Office of Science User Facility under contract no. DE-AC02-05CH11231.

### REFERENCES

- (1) Yan, B.; Felser, C. Topological Materials: Weyl Semimetals. *Annu. Rev. Condens. Matter Phys.* **2017**, *8*, 337–354.
- (2) Schoop, L. M.; Pielhofer, F.; Lotsch, B. V. Chemical Principles of Topological Semimetals. *Chem. Mater.* **2018**, *30* (10), 3155–3176.
- (3) Kumar, N.; Guin, S. N.; Manna, K.; Shekhar, C.; Felser, C. Topological Quantum Materials from the Viewpoint of Chemistry. *Chem. Rev.* **2021**, *121* (5), 2780–2815.
- (4) Nielsen, H. B.; Ninomiya, M. The Adler-Bell-Jackiw anomaly and Weyl fermions in a crystal. *Phys. Lett. B* **1983**, *130* (6), 389–396.
- (5) Vu, D.; Zhang, W.; Şahin, C.; Flatté, M. E.; Trivedi, N.; Heremans, J. P. Thermal chiral anomaly in the magnetic-field-induced ideal Weyl phase of Bi<sub>1-x</sub>Sb<sub>x</sub>. *Nat. Mater.* **2021**, *20* (11), 1525–1531.
- (6) Kang, J. S.; Vu, D.; Zhu, M.; Heremans, J. P. Large and Optimized Thermal Chiral Anomaly in Weyl Semimetal Bi-Sb. *Phys. Rev. Appl.* **2023**, *20* (3), 034014.
- (7) Hermann, W. Elektron und Gravitation. I. *Z. Phys.* **1929**, *56* (5–6), 330–352.
- (8) Belopolski, I.; Manna, K.; Sanchez, D. S.; Chang, G.; Ernst, B.; Yin, J.; Zhang, S. S.; Cochran, T.; Shumiya, N.; Zheng, H.; Singh, B.; Bian, G.; Multer, D.; Litskevich, M.; Zhou, X.; Huang, S.-M.; Wang, B.; Chang, T.-R.; Xu, S.-Y.; Bansil, A.; Felser, C.; Lin, H.; Hasan, M. Z. Discovery of topological Weyl fermion lines and drumhead surface states in a room temperature magnet. *Science* **2019**, *365* (6459), 1278–1281.
- (9) Kuroda, K.; Tomita, T.; Suzuki, M.-T.; Bareille, C.; Nugroho, A.-A.; Goswami, P.; Ochi, M.; Ikhlas, M.; Nakayama, M.; Akebi, S.; Noguchi, R.; Ishii, R.; Inami, N.; Ono, K.; Kumigashira, H.; Varykhalov, A.; Muro, T.; Koretsune, T.; Arita, R.; Shin, S.; Kondo, T.; Nakatsuji, S. Evidence for magnetic Weyl fermions in a correlated metal. *Nat. Mater.* **2017**, *16* (11), 1090–1095.
- (10) Lei, S.; Allen, K.; Huang, J.; Moya, J. M.; Wu, T. C.; Casas, B.; Zhang, Y.; Oh, J. S.; Hashimoto, M.; Lu, D.; Denlinger, J.; Jozwiak, C.; Bostwick, A.; Rotenberg, E.; Balicas, L.; Birgeneau, R.; Foster, M. S.; Yi, M.; Sun, Y.; Morosan, E. Weyl nodal ring states and Landau quantization with very large magnetoresistance in square-net magnet EuGa<sub>4</sub>. *Nat. Commun.* **2023**, *14* (1), 5812.
- (11) Yan, J. Q.; Zhang, Q.; Heitmann, T.; Huang, Z.; Chen, K. Y.; Cheng, J. G.; Wu, W.; Vaknin, D.; Sales, B. C.; McQueeney, R. J. Crystal growth and magnetic structure of MnBi<sub>2</sub>Te<sub>4</sub>. *Phys. Rev. Mater.* **2019**, *3* (6), 064202.
- (12) Vu, D. D.; Nelson, R. A.; Wooten, B. L.; Barker, J.; Goldberger, J. E.; Heremans, J. P. Magnon gap mediated lattice thermal conductivity in MnBi<sub>2</sub>Te<sub>4</sub>. *Phys. Rev. B* **2023**, *108* (14), 144402.
- (13) Rahn, M. C.; Soh, J. R.; Francoal, S.; Veiga, L. S. I.; Stremper, J.; Mardegan, J.; Yan, D. Y.; Guo, Y. F.; Shi, Y. G.; Boothroyd, A. T. Coupling of magnetic order and charge transport in the candidate Dirac semimetal EuCd<sub>2</sub>As<sub>2</sub>. *Phys. Rev. B* **2018**, *97* (21), 214422.
- (14) Schellenberg, I.; Pfannenschmidt, U.; Eul, M.; Schwickert, C.; Pöttgen, R. A <sup>121</sup>Sb and <sup>151</sup>Eu Mössbauer Spectroscopic Investigation of EuCd<sub>2</sub>X<sub>2</sub> (X = P, As, Sb) and YbCd<sub>2</sub>Sb<sub>2</sub>. *Z. Anorg. Allg. Chem.* **2011**, *637* (12), 1863–1870.
- (15) Soh, J. R.; de Juan, F.; Vergniory, M. G.; Schröter, N. B. M.; Rahn, M. C.; Yan, D. Y.; Jiang, J.; Bristow, M.; Reiss, P.; Blandy, J. N.; Guo, Y. F.; Shi, Y. G.; Kim, T. K.; McCollam, A.; Simon, S. H.; Chen, Y.; Coldea, A. I.; Boothroyd, A. T. Ideal Weyl semimetal induced by magnetic exchange. *Phys. Rev. B* **2019**, *100* (20), 201102.
- (16) Jo, N. H.; Kuthanazhi, B.; Wu, Y.; Timmons, E.; Kim, T.-H.; Zhou, L.; Wang, L.-L.; Ueland, B. G.; Palasyuk, A.; Ryan, D. H.; McQueeney, R. J.; Lee, K.; Schruk, B.; Burkov, A. A.; Prozorov, R.

- Bud'ko, S. L.; Kaminski, A.; Canfield, P. C. Manipulating magnetism in the topological semimetal  $\text{EuCd}_2\text{As}_2$ . *Phys. Rev. B* **2020**, *101* (14), 140402.
- (17) Wang, Y.; Li, C.; Li, Y.; Zhou, X.; Wu, W.; Yu, R.; Zhao, J.; Yin, C.; Shi, Y.; Jin, C.; Luo, J.; Zhao, L.; Xiang, T.; Liu, G.; Zhou, X. J. Long-Time Magnetic Relaxation in Antiferromagnetic Topological Material  $\text{EuCd}_2\text{As}_2$ . *Chin. Phys. Lett.* **2021**, *38* (7), 077201.
- (18) Gati, E.; Bud'ko, S. L.; Wang, L.-L.; Valadkhani, A.; Gupta, R.; Kuthanazhi, B.; Xiang, L.; Wilde, J. M.; Sapkota, A.; Guguchia, Z.; Khasanov, R.; Valenti, R.; Canfield, P. C. Pressure-induced ferromagnetism in the topological semimetal  $\text{EuCd}_2\text{As}_2$ . *Phys. Rev. B* **2021**, *104* (15), 155124.
- (19) Chen, X.; Wang, S.; Wang, J.; An, C.; Zhou, Y.; Chen, Z.; Zhu, X.; Zhou, Y.; Yang, Z.; Tian, M. Temperature-pressure phase diagram of the intrinsically insulating topological antiferromagnet  $\text{EuCd}_2\text{As}_2$ . *Phys. Rev. B* **2023**, *107* (24), L241106.
- (20) Kuthanazhi, B.; Joshi, K. R.; Ghimire, S.; Timmons, E.; Wang, L.-L.; Gati, E.; Xiang, L.; Prozorov, R.; Bud'ko, S. L.; Canfield, P. C. Magnetism and T-x phase diagrams of Na- and Ag-substituted  $\text{EuCd}_2\text{As}_2$ . *Phys. Rev. Mater.* **2023**, *7* (3), 034402.
- (21) Ma, J.; Wang, H.; Nie, S.; Yi, C.; Xu, Y.; Li, H.; Jandke, J.; Wulfhchel, W.; Huang, Y.; West, D.; Richard, P.; Chikina, A.; Strocov, V. N.; Mesot, J.; Weng, H.; Zhang, S.; Shi, Y.; Qian, T.; Shi, M.; Ding, H. Emergence of Nontrivial Low-Energy Dirac Fermions in Antiferromagnetic  $\text{EuCd}_2\text{As}_2$ . *Adv. Mater.* **2020**, *32* (14), 1907565.
- (22) Ma, J.-Z.; Nie, S. M.; Yi, C. J.; Jandke, J.; Shang, T.; Yao, M. Y.; Naamneh, M.; Yan, L. Q.; Sun, Y.; Chikina, A.; Strocov, V. N.; Medarde, M.; Song, M.; Xiong, Y.-M.; Xu, G.; Wulfhchel, W.; Mesot, J.; Reticcioli, M.; Franchini, C.; Mudry, C.; Müller, M.; Shi, Y. G.; Qian, T.; Ding, H.; Shi, M. Spin fluctuation induced Weyl semimetal state in the paramagnetic phase of  $\text{EuCd}_2\text{As}_2$ . *Sci. Adv.* **2019**, *5* (7), No. eaaw4718.
- (23) Wang, H. P.; Wu, D. S.; Shi, Y. G.; Wang, N. L. Anisotropic transport and optical spectroscopy study on antiferromagnetic triangular lattice  $\text{EuCd}_2\text{As}_2$ : An interplay between magnetism and charge transport properties. *Phys. Rev. B* **2016**, *94* (4), 045112.
- (24) Liu, D. F.; Liang, A. J.; Liu, E. K.; Xu, Q. N.; Li, Y. W.; Chen, C.; Pei, D.; Shi, W. J.; Mo, S. K.; Dudin, P.; Kim, T.; Cacho, C.; Li, G.; Sun, Y.; Yang, L. X.; Liu, Z. K.; Parkin, S. S. P.; Felser, C.; Chen, Y. L. Magnetic Weyl semimetal phase in a Kagomé crystal. *Science* **2019**, *365* (6459), 1282–1285.
- (25) Du, F.; Yang, L.; Nie, Z.; Wu, N.; Li, Y.; Luo, S.; Chen, Y.; Su, D.; Smidman, M.; Shi, Y.; Cao, C.; Steglich, F.; Song, Y.; Yuan, H. Consecutive topological phase transitions and colossal magnetoresistance in a magnetic topological semimetal. *npj Quantum Mater.* **2022**, *7* (1), 65.
- (26) Roychowdhury, S.; Yao, M.; Samanta, K.; Bae, S.; Chen, D.; Ju, S.; Raghavan, A.; Kumar, N.; Constantinou, P.; Guin, S. N.; Plumb, N. C.; Romanelli, M.; Borrmann, H.; Vergniory, M. G.; Strocov, V. N.; Madhavan, V.; Shekhar, C.; Felser, C. Anomalous Hall Conductivity and Nernst Effect of the Ideal Weyl Semimetallic Ferromagnet  $\text{EuCd}_2\text{As}_2$ . *Adv. Sci.* **2023**, *10* (13), 2207121.
- (27) Sanjeeva, L. D.; Xing, J.; Taddei, K. M.; Parker, D.; Custelcean, R.; dela Cruz, C.; Sefat, A. S. Evidence of Ba-substitution induced spin-canting in the magnetic Weyl semimetal  $\text{EuCd}_2\text{As}_2$ . *Phys. Rev. B* **2020**, *102* (10), 104404.
- (28) Xu, Y.; Das, L.; Ma, J. Z.; Yi, C. J.; Nie, S. M.; Shi, Y. G.; Tiwari, A.; Tsirkin, S. S.; Neupert, T.; Medarde, M.; Shi, M.; Chang, J.; Shang, T. Unconventional Transverse Transport above and below the Magnetic Transition Temperature in Weyl Semimetal  $\text{EuCd}_2\text{As}_2$ . *Phys. Rev. Lett.* **2021**, *126* (7), 076602.
- (29) Cao, X.; Yu, J.-X.; Leng, P.; Yi, C.; Chen, X.; Yang, Y.; Liu, S.; Kong, L.; Li, Z.; Dong, X.; Shi, Y.; Bibes, M.; Peng, R.; Zang, J.; Xiu, F. Giant nonlinear anomalous Hall effect induced by spin-dependent band structure evolution. *Phys. Rev. Res.* **2022**, *4* (2), 023100.
- (30) Yu, Z.; Chen, X.; Xia, W.; Wang, N.; Lv, X.; Wu, D.; Wu, W.; Liu, Z.; Zhao, J.; Li, M.; Li, S.; Li, X.; Dong, Z.; Zhou, C.; Zhang, L.; Wang, X.; Yu, N.; Zou, Z.; Luo, J.; Cheng, J.; Wang, L.; Zhong, Z.; Guo, Y. Structure, Magnetotransport, and Theoretical Study on the Layered Antiferromagnet Topological Phase  $\text{EuCd}_2\text{As}_2$  under High Pressure. *Adv. Quantum Technol.* **2023**, *6* (5), 2200128.
- (31) Shi, Y.; Liu, Z.; Burnett, L. A.; Lee, S.; Hu, C.; Jiang, Q.; Cai, J.; Xu, X.; Li, M.; Chen, C.-C.; Chu, J.-H. Absence of Weyl nodes in  $\text{EuCd}_2\text{As}_2$  revealed by the carrier density dependence of the anomalous Hall effect. *Phys. Rev. B* **2024**, *109* (12), 125202.
- (32) Jo, N. H.; Wu, Y.; Trevisan, T. V.; Wang, L.-L.; Lee, K.; Kuthanazhi, B.; Schrunck, B.; Bud'ko, S. L.; Canfield, P. C.; Orth, P. P.; Kaminski, A. Visualizing band selective enhancement of quasiparticle lifetime in a metallic ferromagnet. *Nat. Commun.* **2021**, *12* (1), 7169.
- (33) Nishihaya, S.; Nakamura, A.; Ohno, M.; Kriener, M.; Watanabe, Y.; Kawasaki, M.; Uchida, M. Intrinsic insulating transport characteristics in low-carrier density  $\text{EuCd}_2\text{As}_2$  films. *Appl. Phys. Lett.* **2024**, *124* (2), 023103.
- (34) Wang, Y.; Li, C.; Miao, T.; Zhang, S.; Li, Y.; Zhou, L.; Yang, M.; Yin, C.; Cai, Y.; Song, C.; Luo, H.; Chen, H.; Mao, H.; Zhao, L.; Deng, H.; Sun, Y.; Zhu, C.; Zhang, F.; Yang, F.; Wang, Z.; Zhang, S.; Peng, Q.; Pan, S.; Shi, Y.; Weng, H.; Xiang, T.; Xu, Z.; Zhou, X. J. Giant and reversible electronic structure evolution in a magnetic topological material  $\text{EuCd}_2\text{As}_2$ . *Phys. Rev. B* **2022**, *106* (8), 085134.
- (35) Santos-Cottin, D.; Mohelský, J.; Wyzula, J.; Le Mardele, F.; Kapon, I.; Nasrallah, S.; Barišić, N.; Živković, I.; Soh, J. R.; Guo, F.; Rigaux, K.; Puppini, M.; Dil, J. H.; Gudac, B.; Rukelj, Z.; Novak, M.; Kuzmenko, A. B.; Homes, C. C.; Dietl, T.; Orlita, M.; Akrap, A.  $\text{EuCd}_2\text{As}_2$ : A Magnetic Semiconductor. *Phys. Rev. Lett.* **2023**, *131* (18), 186704.
- (36) Kuzmany, H. The Dielectric Response Functions. In *Solid-State Spectroscopy: An Introduction*; Springer: Berlin Heidelberg, 2009; pp 107–127.
- (37) Wang, Y.; Ma, J.; Yuan, J.; Wu, W.; Zhang, Y.; Mou, Y.; Gu, J.; Cheng, P.; Shi, W.; Yuan, X.; Zhang, J.; Guo, Y.; Zhang, C. Absence of metallicity and bias-dependent resistivity in low-carrier-density  $\text{EuCd}_2\text{As}_2$ . *Sci. China: Phys., Mech. Astron.* **2024**, *67* (4), 247311.
- (38) Tansley, T. L.; Foley, C. P. Optical band gap of indium nitride. *J. Appl. Phys.* **1986**, *59* (9), 3241–3244.
- (39) Davydov, V. Y.; Klochikhin, A. A.; Emtsev, V. V.; Ivanov, S. V.; Vekshin, V. V.; Bechstedt, F.; Furthmüller, J.; Harima, H.; Mudryi, A. V.; Hashimoto, A.; Yamamoto, A.; Aderhold, J.; Graul, J.; Haller, E. E. Band Gap of InN and In-Rich  $\text{In}_x\text{Ga}_{1-x}\text{N}$  alloys ( $0.36 < x < 1$ ). *Phys. Status Solidi B* **2002**, *230* (2), R4–R6.
- (40) Monemar, B.; Paskov, P. P.; Kasic, A. Optical properties of InN—the bandgap question. *Superlattices Microstruct.* **2005**, *38* (1), 38–56.
- (41) Cuono, G.; Sattigeri, R. M.; Autieri, C.; Dietl, T. Ab initio overestimation of the topological region in Eu-based compounds. *Phys. Rev. B* **2023**, *108* (7), 075150.
- (42) Canfield, P. C.; Fisk, Z. Growth of single crystals from metallic fluxes. *Philos. Mag. B* **1992**, *65* (6), 1117–1123.
- (43) Canfield, P. C.; Kong, T.; Kaluarachchi, U. S.; Jo, N. H. Use of frit-disc crucibles for routine and exploratory solution growth of single crystalline samples. *Philos. Mag.* **2016**, *96* (1), 84–92.
- (44) Katoch, J.; Ulstrup, S.; Koch, R. J.; Moser, S.; McCreary, K. M.; Singh, S.; Xu, J.; Jonker, B. T.; Kawakami, R. K.; Bostwick, A.; Rotenberg, E.; Jozwiak, C. Giant spin-splitting and gap renormalization driven by trions in single-layer  $\text{WS}_2/\text{h-BN}$  heterostructures. *Nat. Phys.* **2018**, *14* (4), 355–359.
- (45) Artmann, A.; Mewis, A.; Roepke, M.; Michels, G.  $\text{AM}_2\text{X}_2$ -Verbindungen mit  $\text{CaAl}_2\text{Si}_2$ -Struktur. XI. Struktur und Eigenschaften der Verbindungen  $\text{ACd}_2\text{X}_2$  (A: Eu, Yb; X: P, As, Sb). *Z. Anorg. Allg. Chem.* **1996**, *622* (4), 679–682.
- (46) Soh, J. R.; Schierle, E.; Yan, D. Y.; Su, H.; Prabhakaran, D.; Weschke, E.; Guo, Y. F.; Shi, Y. G.; Boothroyd, A. T. Resonant x-ray scattering study of diffuse magnetic scattering from the topological semimetals  $\text{EuCd}_2\text{As}_2$  and  $\text{EuCd}_2\text{Sb}_2$ . *Phys. Rev. B* **2020**, *102* (1), 014408.
- (47) Sun, Y.; Li, Y.; Li, S.; Yi, C.; Deng, H.; Du, X.; Liu, L.; Zhu, C.; Li, Y.; Wang, Z.; Mao, H.; Shi, Y.; Wu, R. Experimental evidence for field-induced metamagnetic transition of  $\text{EuCd}_2\text{As}_2$ . *J. Rare Earths* **2022**, *40* (10), 1606–1610.

(48) Jose, G. C.; Burrage, K.; Jimenez, J. L. G.; Xie, W.; Lavina, B.; Zhao, J.; Alp, E. E.; Zhang, D.; Xiao, Y.; Vohra, Y. K.; Bi, W. Evolution of magnetism, valence, and crystal lattice in  $\text{EuCd}_2\text{As}_2$  under pressure. *Phys. Rev. B* **2023**, *107* (24), 245121.

(49) Toby, B. H.; Von Dreele, R. B. GSAS-II: the genesis of a modern open-source all purpose crystallography software package. *J. Appl. Crystallogr.* **2013**, *46* (2), 544–549.

(50) Fritzsche, H. Resistivity and hall coefficient of antimony-doped germanium at low temperatures. *J. Phys. Chem. Solids* **1958**, *6* (1), 69–80.

(51) Kittel, C.; McEuen, P. *Introduction to Solid State Physics*; John Wiley & Sons, 2018.

(52) Jovovic, V.; Thiagarajan, S.; West, J.; Heremans, J.; Story, T.; Golacki, Z.; Paszkowicz, W.; Osinniy, V. Transport and magnetic properties of dilute rare-earth–PbSe alloys. *J. Appl. Phys.* **2007**, *102* (4), 043707.

(53) Arguilla, M. Q.; Cultrara, N. D.; Baum, Z. J.; Jiang, S.; Ross, R. D.; Goldberger, J. E.  $\text{EuSn}_2\text{As}_2$ : an exfoliatable magnetic layered Zintl–Klemm phase. *Inorg. Chem. Front.* **2017**, *4* (2), 378–386.

(54) Zong, Y.; Fujita, K.; Akamatsu, H.; Murai, S.; Tanaka, K. Antiferromagnetism of perovskite  $\text{EuZrO}_3$ . *J. Solid State Chem.* **2010**, *183* (1), 168–172.

(55) Fender, S. S.; Thomas, S. M.; Ronning, F.; Bauer, E. D.; Thompson, J. D.; Rosa, P. F. S. Narrow-gap semiconducting behavior in antiferromagnetic  $\text{Eu}_{11}\text{InSb}_9$ . *Phys. Rev. Mater.* **2021**, *5* (7), 074603.

(56) Janowitz, C.; Scherer, V.; Mohamed, M.; Krapf, A.; Dwelk, H.; Manzke, R.; Galazka, Z.; Uecker, R.; Irmischer, K.; Fornari, R.; Michling, M.; Schmeißer, D.; Weber, J. R.; Varley, J. B.; Walle, C. G. V. d. Experimental electronic structure of  $\text{In}_2\text{O}_3$  and  $\text{Ga}_2\text{O}_3$ . *New J. Phys.* **2011**, *13* (8), 085014.